Toward a chemical control of colloidal YVO4 nanoparticles microstructure

Marie-Alexandra Neouze, Alexy Freitas, Raj-Kumar Ramamoorthy, Rabei Mohammedi, Eric Larquet, Sandrine Tusseau-Nenez, David Carriere, Thierry Gacoin

Toward a chemical control of colloidal YVO_4 nanoparticles microstructure

Marie-Alexandra Neouze,[1,2,†,§] Alexy P. Freitas,[1,2,§] Raj-Kumar Ramamoorthy, [2,#] Rabei Mohammedi,[1] Eric Larquet,[1] Sandrine Tusseau-Nenez[1], David Carrière,[2] Thierry Gacoin[1*]*

[1] Laboratoire de Physique de la Matière Condensée, Ecole Polytechnique, CNRS, Université Paris-Saclay, Route de Saclay, 91128 Palaiseau cedex (France).

[2] NIMBE, CEA, CNRS, Université Paris-Saclay, CEA Saclay 91191 Gif sur Yvette Cedex

KEYWORDS: vanadate nanoparticles - co-precipitation - nanocrystals - SAXS - microstructure.

Abstract.

Rare earth doped oxides are a class of compounds that have been largely studied in the context of the development of luminescent nanocrystals for various applications including fluorescent labels for bio-imaging, MRI contrast agents, luminescent nanocomposite coatings etc. Elaboration of colloidal suspensions is usually achieved through coprecipitation. Particles exhibit emission properties that are similar to the bulk counterparts, although altered by crystalline

defects or surface quenching species. Focusing on YVO_4:Eu, one of the first reported systems, the aim of this work is to revisit the elaboration of nanoparticles obtained through a simple aqueous coprecipitation route. The objective is more precisely to get a better understanding of the parameters affecting the particles' internal microstructure, a feature that is poorly controlled and characterized. We show that the hydroxyl concentration in the precursor solution has a drastic effect on the particles' microstructure. Moreover, discrepancies in the reported particles structure are shown to possibly arise from a carbonation of the strongly basic orthovanadate precursor. For this study, SAXS/WAXS is shown to be a powerful tool to characterize the multiscale structure of the particles. It could be shown that playing on the precursor composition, it may be varied between almost monocrystalline nanocrystals to particles exhibiting a hierarchical microstructure well described by a surface fractal model. This work provides a new methodology for the characterization of nanoparticles microstructure, and opens new directions for its optimization in view of applications.

Introduction.

In the context of the development of light emitting nanoparticles, rare earth doped oxides appear as appealing systems considering their high emission yield, their simple functionalization and their interesting spectroscopic features such as narrow emission lines for f transitions, tunable emission wavelength by playing on the rare earth dopant, possible up-conversion emission [1], etc. YVO_4:Eu has been among the first reported systems, mainly because the bulk material exhibits high emission yield [2] and crystalline nanoparticles can be quite easily prepared through conventional colloidal chemistry from aqueous precursor salts [3, 4]. As such, original

applications were investigated in various fields such as light emitting coatings [5,6], biolabels for luminescence imaging and sensors [7-9] - or more recently as contrast agent in Magnetic Resonance Imaging (MRI) [10].

The development of optimized elaboration processes is a very important issue in order to obtain stable dispersions of colloidal particles with a controlled size and enhanced emission properties. In this field, the main issue is to obtain particles exhibiting the highest emission yield considering the detrimental impact of surface quenching (especially by surface hydroxyls) or the presence of crystalline defects, grains boundaries and even porosity [11, 12]. However, particles with a high specific area might be preferred for other applications such as chemical sensors or relaxing agents for MRI which require optimized interactions with the surrounding chemical environment. A compromise between the best emission properties on the one hand and the best surface sensitivity on the other hand thus requires developing chemical syntheses of nanoparticles with a well-controlled microstructure, not only toward a perfect monocristallinity.

Many papers have reported the influence of some parameters of elaboration on the particles' morphology, evidencing the role of pH, thermal conditions of elaboration (hydrothermal synthesis or microwave heating), addition of surfactants, or complexing agents [9, 13-17]. Fewer works have concerned the detailed analysis of the particles' internal microstructure in term of polycrystalline arrangement, crystalline defects or porosity. These features appear to be poorly controlled and the link with experimental parameters is both unclear and unreproducible. Such a poor control of the synthesis was also evidenced by our observation that simple change in the sodium orthovanadate precursor batch leads to particles with significantly different microstructures as probed by their coherence lengths (Table S1 in the Supporting Information).

Following our previous investigation [18] on the mechanism of the particles' formation by aqueous coprecipitation, which evidenced the template role of an amorphous phase, the present work aims in revisiting the elaboration process of YVO_4 nanoparticles using perfectly controlled experimental initial conditions. We decided to start from sodium metavanadate $NaVO_3$ instead of the orthovanadate Na_3VO_4, which has been commonly used by us and many others. The goal is to have a perfect control of the pH, monitored as the number of equivalents of NaOH with respect to $NaVO_3$. Moreover, suspecting a significant influence of carbonates present in the alkaline orthovanadate precursors (Table S1 in the Supporting Information), we also decided to investigate the impact of this specific additive. Playing on the alkalinity of the solutions and the presence of carbonates, the structure of the obtained particles was fully characterized using X-ray diffraction (XRD) and transmission electron microscopy (TEM), but also using small- and wide-angle X-ray scattering (SAXS-WAXS) of the solution without prior drying, thus providing a complete multiscale characterization of the particles. We evidenced the drastic influence of the investigated chemical parameters on the particles' structure, thus offering a convenient and reproducible way for its control toward optimized properties.

Experimental Section

YVO_4:Eu nanoparticles elaboration. Unless otherwise specified, all powder precursors ($NaVO_3$, Na_2CO_3, $Y(NO_3)_3.6H_2O$, $Eu(NO_3)_3.5H_2O$) have been purchased from Sigma-Aldrich and used as such in MilliQ water. All steps of the synthesis are achieved under ambient conditions. In a typical synthesis, a first aqueous solution is prepared with $NaVO_3$ (0.1 $mol.L^{-1}$) and the appropriate amount of NaOH (2 or 3 equivalents with respect to $NaVO_3$, from a fresh aqueous 1M stock solution, Fixanal) and Na_2CO_3 (0 or 1 equivalent with respect to $NaVO_3$) is

added. The carbonate content in the metavanadate solutions was found below sensitivity of the carbonate specific electrode (Orion™ 9502BNWP), estimated to the micromolar range. A second aqueous solution is prepared with $Y(NO_3)_3$ (0.08 $mol.L^{-1}$) and $Eu(NO_3)_3$ (0.02 $mol.L^{-1}$). In a second step, 25 mL of each solution are mixed rapidly and left under vigorous stirring for 12 days prior to analysis.

Structural characterizations. Powder X-ray diffraction (XRD) experiments were carried out with a Bragg-Brentano geometry diffractometer (X'Pert PANalytical) equipped with a Cu tube ($K_{\alpha 1}$ and $K_{\alpha 2}$ wavelengths) and the X'Celerator detector. A careful preparation of the sample was achieved in order to prevent any structural change to occur through recovering the particles as a dried powder. 10 mL of the colloidal suspension are mixed with 10 mL of ethanol. The mixture is centrifuged (3 min. 13000 g) and the precipitate is mixed again with 20 mL ethanol then centrifuged again. The precipitate is then dispersed in 20 mL of acetone and centrifuged for a third time. The supernatant is discarded and the precipitate is left for drying under ambient conditions.

TEM observations. Transmission Electron Microscopy (TEM) observations were carried out with a JEOL JEM-2010F microscope operating at 200 kV accelerating voltage with a high-resolution HR polar piece (Cs = 1.4 mm, point resolution = 0.21 nm). Images were collected with a 4Kx4K GATAN 794 CCD camera. 20µL droplets of water diluted particles were successively positioned on an individual Parafilm line. Using a specimen grid coated with an appropriately positive glow-discharge treated carbon, the grid is put in contact with the sample droplet by capillarity. After allowing one minute for adsorption of the sample on the carbon, the grid was removed and rapidly washed (30 sec) sequentially with two droplets of distilled water.

The fluid in excess is then removed by carefully placing a filter paper wedge onto the edge of the grid, followed by air-drying.

X-ray scattering characterizations. Small and wide angle X-ray scattering (SAXS/WAXS) measurements have been performed at a wavelength of 12.5 keV both on the ID02 beamline at the ESRF synchrotron facility [19] and at the Swing beamline at SOLEIL [20]. On ID02, two CCD detectors were used for simultaneous collection of SAXS and WAXS at respective distances of 160 cm ($q \leq 0.6$ Å^{-1}) and 13 cm ($q \geq 0.6$ Å^{-1}). On Swing, two sample–detector distances of 6.3 m and 58 cm were used, leading to a range of $q = 5.6 \times 10^{-3}$ Å^{-1} to 3.1 Å^{-1}. On the ID02 beamline, the nanoparticles were stabilized against sedimentation by several centrifugations/redispersions in water, and by addition of ammonium poly(acrylate). On the Swing beamline, pristine solutions without stabilization were used, with less than a minute between introduction in the glass capillary and the end of the acquisition. Model fitting has been performed using a home-made script written in Python language, as detailed in Supplementary Information. The standard deviation on the fit parameters and derived physical constants (e.g. the specific area) have been estimated with the resampling ("bootstrapping") method [21]: in order to reproduce and propagate the experimental uncertainty, the fits and calculations were performed over a series of 100 datasets randomly generated around the experimental dataset, with a variance equal to the experimental standard deviation. The 95% confidence interval was obtained from the histogram of the parameters of interest.

Results and Discussion

Particle synthesis. This work aims to precisely understand the influence of chemical parameters on the microstructure of YVO_4 obtained by coprecipitation from precursor salts in

aqueous solutions. It is admitted from several studies that the pH has a drastic influence through determining the precipitation of an amorphous hydroxylated precipitate which structure may influence the final particle microstructure [18]. Due to the speciation of the vanadate species [22, 23], YVO_4 is obtained at rather high pH (typically higher than 12). This pH is mainly imposed by the orthovanadate when using this precursor, but can be adjusted through the addition of a base either before or during the precipitation. However, because the molarity of hydroxyl ions is log-dependent on the pH, the latter is actually a poor indicator of the former in extremely basic media (typically pH ~13). Also, discrepancies were found in the natural pH of orthovanadate solutions depending on the supplier or lot number leading to particles with variable structures (Table S1 in the Supporting Information). Hypothesis is made that this could arise from a partial carbonation of the orthovanadate powder either from the supplier or during its storage, favored by its basic character. This was confirmed through the measurement of the carbonate content in solutions made using orthovanadate from different suppliers: results (Table S1 in the Supporting Information) indeed evidenced a significant amount of carbonates in almost all precursor batches, exhibiting a CO_3^{2-}/V molar ratio comprised between 0.06 and 0.72.

In order to have a precise understanding of the influence of pH and carbonates on the microstructure of the YVO_4 nanoparticles, we thus decided to use a metavanadate precursor ($NaVO_3$) which stoichiometry is well controlled and which has a much lower tendency toward carbonation (a 0.1 $mol.L^{-1}$ solution has a pH of 7.9). The carbonate content in the metavanadate solutions was found below the detection limit of a carbonate-specific electrode, estimated to the micromolar range. It is, as expected, orders of magnitude lower than for solutions prepared from orthovanadate precursors. Although the speciation of vanadate in solution may be rather complex [23], one can assume that at least two equivalents of NaOH must be added to the vanadate

precursor in order to ensure conversion into the orthovanadate (VO_3^- + 2 OH^- –> VO_4^{3-} + H_2O). Na_2CO_3 was also optionally added to the vanadate precursor. This preparation allows for the precipitation of the YVO_4 under similar conditions as if partially carbonated Na_3VO_4 had been used, but with a precisely controlled composition of the precursor solution.

Table 1 summarizes the investigated compositions, (named YV2, YV2C, YV3 and YV3C), where YVn refers to the preparation of YVO_4 nanoparticles using n equivalents of NaOH in the vanadate precursor. The addition of carbonates (one equivalent as compared to V) is indicated by the C label.

Sample	**$NaVO_3$** mol.L^{-1}	**NaOH** mol.L^{-1}	Na_2CO_3 mol.L^{-1}	pH	$Y(NO_3)_3$ + $Eu(NO_3)_3$ mol.L^{-1}
YV2	0.1	0.2	0	12.8	0.08 + 0.02
YV2C	0.1	0.2	0.1	12.8	0.08 + 0.02
YV3	0.1	0.3	0	12.9	0.08 + 0.02
YV3C	0.1	0.3	0.1	12.9	0.08 + 0.02

Table 1. Samples name and compositions of the precursor solutions.

X-Ray Diffraction (XRD) structural characterization. Structural characterizations were first achieved using X-ray diffraction from dried powders of nanoparticles. In all samples, crystallization was found to occur from an amorphous hydroxylated phase similarly to what has been described previously [18] but with kinetics that appeared strongly affected by the pH (n value). Qualitative monitoring by XRD (Figure S1 in the Supporting Information) evidenced that the conversion into YVO_4 was completed within a few hours in the case of YV2 and YV2C and only several days in the case of YV3 and YV3C. We here focus on the final particle morphology

as obtained after an ageing time that we fixed to 12 days, which was found necessary to ensure a complete reaction of crystallization for all particles.

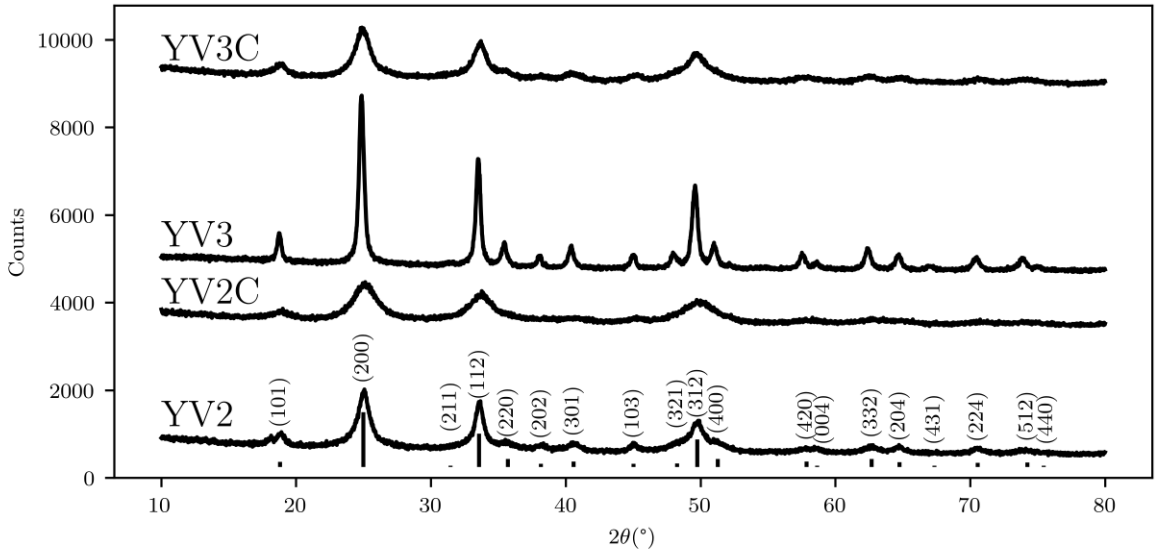

Figure 1. X-ray Diffractograms (Cu K_α) of the four YV2, YV2C, YV3, YV3C samples. Reference vertical lines were calculated from the reference patterns of YVO_4 (ICSD-36060) and $EuVO_4$ (ICSD-81702) assuming the Vegard's law for the $Y_{0.8}Eu_{0.2}VO_4$ composition.

Fig. 1 shows the X-ray diagrams recorded for the four investigated YVO_4 samples. All exhibit the characteristic peaks of the quadratic $I4_1/amd$ zircon (or xenotime) structure, known for the bulk YVO_4 [24] with no detectable parasitic phases. Clear differences are observed considering the peaks broadening, evidencing large differences in the particles' structure depending on the synthetic conditions. Peak broadening may result from different deviation from the bulk monocrystalline material such as limited size effect or microstrains associated to defects. Different approaches of X-ray diagram analysis may be used to get some more quantitative analysis of the particles' structure, also considering some anisotropy effects. Application of the Scherrer law may first be achieved by simply plotting the calculated coherence length L_c from

distinct diffraction peaks as a function of their diffraction angle. The results, shown in Fig.2, shows the large variation of average coherence lengths ranging from 3.8 nm (YV2C) to 23 nm (YV3), with 6.6 nm (YV3C) and 8 nm (YV2).

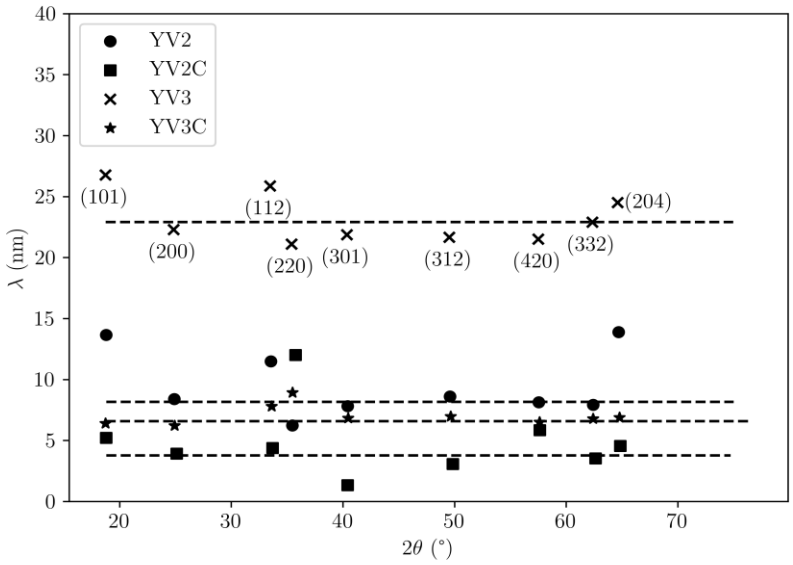

Figure 2. Coherence length for samples YV2, YV2C, YV3, YV3C determined from the Scherrer equation for all peaks observed in the diffraction diagrams (see Fig. 1)

It nevertheless obviously appears that providing an average coherence length can only be a rough estimation, considering the discrepancy of coherence lengths obtained from different peaks. This can be attributed to the effect of some anisotropies of shape and/or microstrains (even if in the Scherrer formula only a size effect was taken into account) along certain direction. Analysis of microstrains using the Williamson-Hall or the Halder-Wagner equations [25,26] (Figures S2 and S3 in the Supporting Information) is also strongly limited by anisotropy. We thus achieved a Rietveld analysis using the MAUD software [27] thus introducing in particular shape anisotropies and lattice parameters as adjustable parameters (Table S2 in the Supporting Information). Acceptable simulations of the experimental diffraction diagrams could be obtained

when considering that the crystallites exhibit a prolate spheroidal shape with adjustable dimensions. Results are provided on Table 2.

Coherence lengths derived from the Rietveld analysis confirm the much higher values observed for the YV3 sample as compared to other samples, especially the carbonated ones. In addition, the crystallites in the YV3 sample appear more isotropic, while the YV2 crystallites - and to a lesser degree the carbonated ones - seem to have a more prolate morphology. These values are in agreement with the sizes calculated from the Scherrer equation, as the level of microstrain is very low (< 1%) whatever the sample.

Lattice parameters are determined from the simulation and compared to those of a synthesized bulk compound with the same Eu content in solid solution. The latter has parameters comparable to those calculated using a linear combination of bulk YVO_4 and $EuVO_4$ [28,29], confirming the good dispersion of the Eu as a solid solution. YV2 sample has parameters very close to those of the bulk, which is not the case of other samples although deviations are not very important.

Sample		Bulk	YV2	YV2C	YV3	YV3C
Lattice parameters	a = b (Å)	7.147	7.140	7.102	7.163	7.152
	c (Å)	6.309	6.302	6.279	6.297	6.273
Average Coherence length L_c (nm)		/	10.6	5.7	26.7	8.8
microstrains		/	0.004	0.020	0.002	0.007
Coherence length along long axis L_c (001)(nm)		/	17.4	8.4	34.6	12.0
Coherence length		/	11.4	6.4	32.4	10.6

along short axis L_c (100)(nm)					
Shape anisotropy L_c (001)/ L_c (100)	/	1.5	1.3	1.1	1.2

Table 2. Structural parameters extracted from XRD patterns using the Rietveld analysis (MAUD software). The average coherence length is the square root of the ellipsoid volume.

TEM Microscopy. Fig. 3 shows typical TEM images for each sample. Clear variations of the microstructures are observed between the different samples. YV2 particles (top-left corner) are rather polydisperse and exhibit a strongly anisotropic shape, thus confirming the conclusion of the XRD analysis. We note that their morphology is similar to the one of many reported YVO_4 nanoparticles from the literature [4, 9, 15], leading to the hypothesis of oriented attachment of anisotropic primary particles.

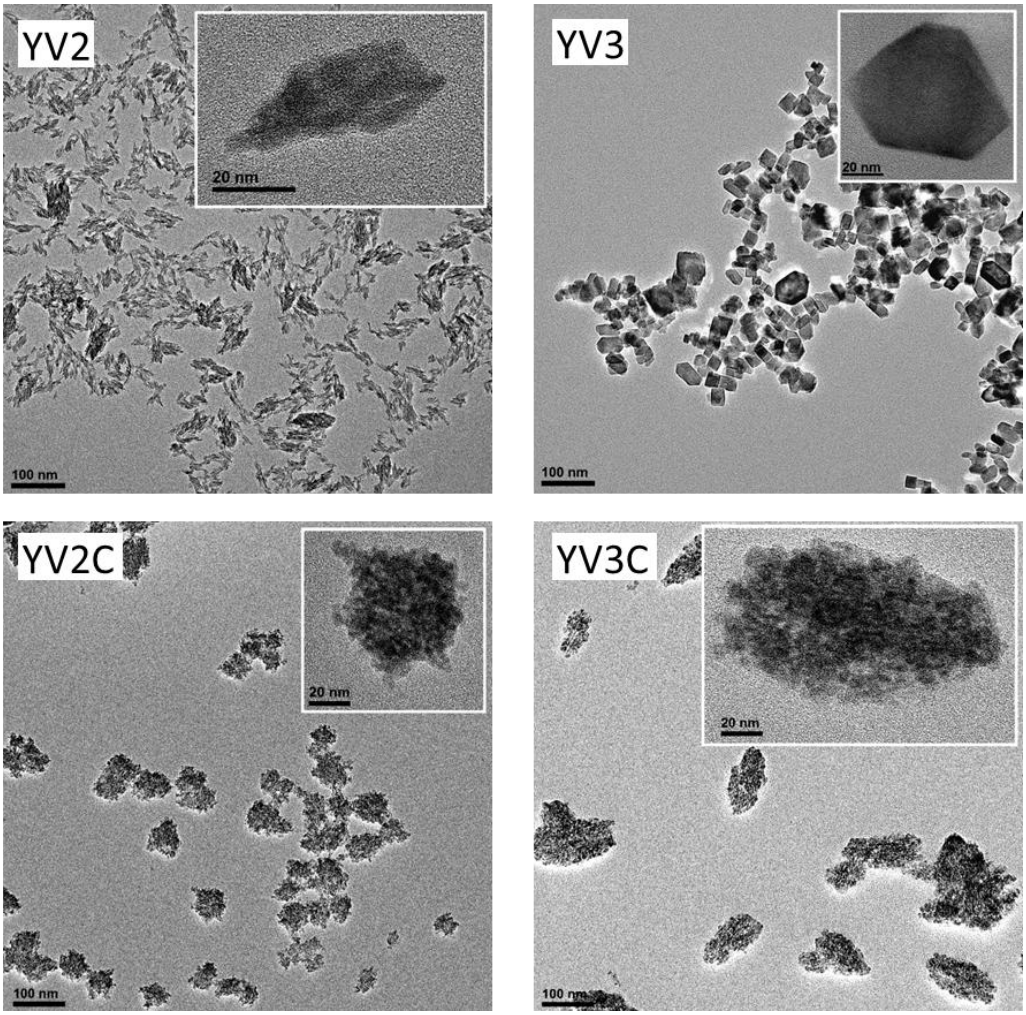

Figure 3. TEM microscopy of the four YV2, YV2C, YV3 and YV3C samples

Images of the YV3 sample confirm its much higher crystallinity, both regarding the contrast homogeneity within the volume of the particles and the crystalline facets. The particles are nevertheless not completely monocrystalline, considering that their size as seen in the TEM pictures (20 to 80 nm) is significantly larger than the coherence length obtained from XRD (around 30 nm).

Samples obtained under the presence of carbonates (YV2C and YV3C) exhibit a similar morphology that seems to result from the aggregation of primary particles which dimensions seem to be compatible with the crystallite size estimated from XRD (less than 10 nm).

Structural characterizations by SAXS/WAXS. The TEM pictures show prominent electron contrast heterogeneities in the YV2, YV2C and YV3C assigned to the roughness of the particles. Modeling of the SAXS and WAXS patterns (Fig. 4) allows specifying the properties of the surface, and in particular measuring the surface area of the particles.

Qualitatively, we observe at low q values an inflexion assigned to the characteristic size of the particles ($q \approx 10^{-2}$ Å^{-1}, diameter ≈ 10 nm), followed by an inflexion characteristic of smaller grains that constitute the particles ($q \approx 10^{-1}$ Å^{-1}, diameter ≈ 1 nm). The magnitude of the latter signal varies as expected from the TEM observations: the signal of the primary grains is well resolved for the YV2C and YV3C syntheses, remains observable for the YV2 syntheses, but is hardly observed for the YV3 syntheses. Between both signals, the scattered intensity decays as a q^{-p} law with $p < 4$ (Fig. 4, dotted lines), that is characteristic of the roughness induced by the aggregation of the primary grains into the nanoparticles.

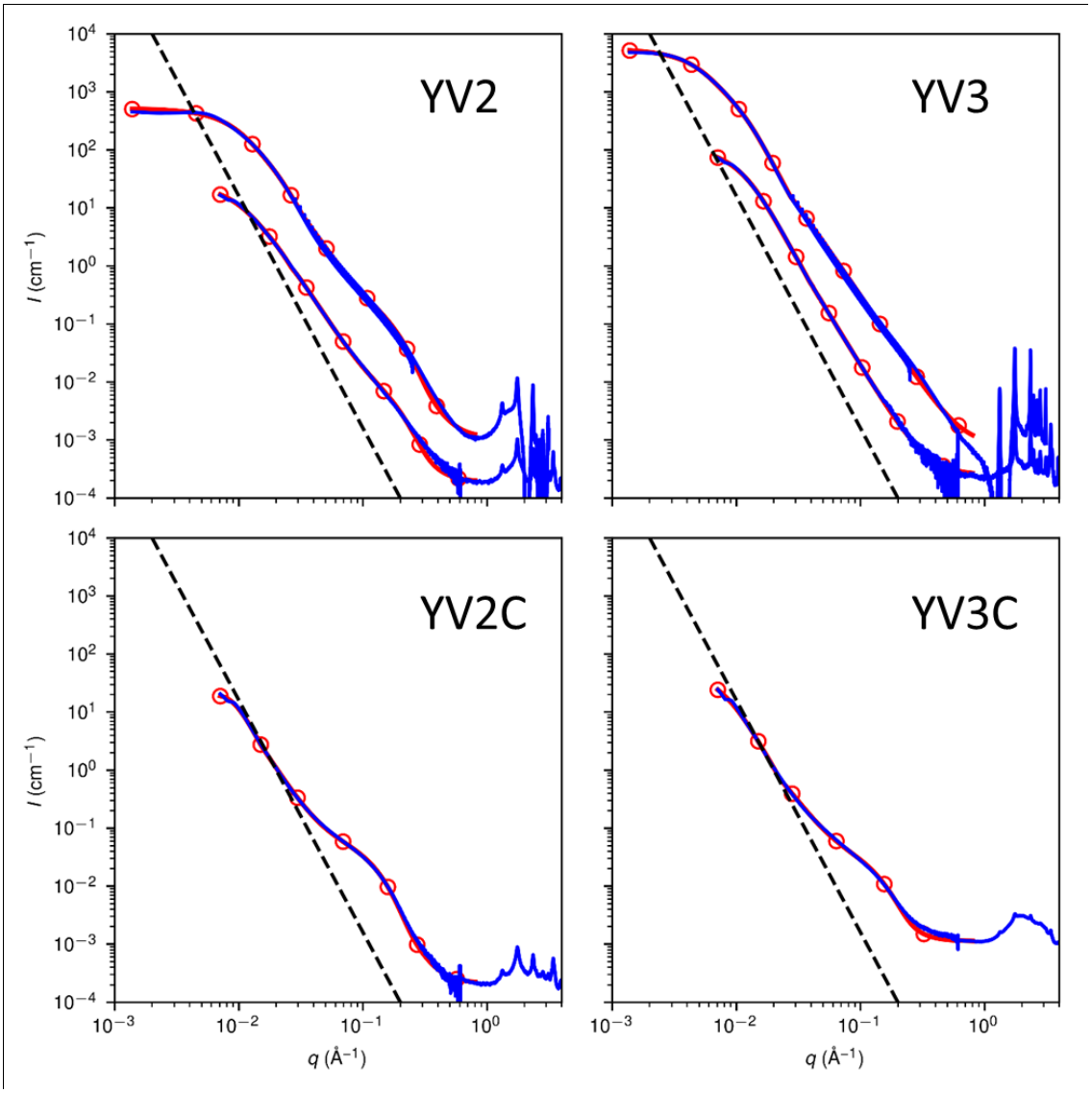

Figure 4. Small- and wide-angle X ray scattering patterns of a) YV2, b) YV3, c) YV2C and d) YV3C nanoparticle dispersions. The dotted line indicates a q^{-4} decay characteristic of objects with a smooth interface (Porod's law). The red lines and symbols are the best fit of surface fractal models. The datasets with the lowest *q* values have been recorded at the SOLEIL/Swing beamline. The datasets with the highest *q* values have been recorded at the ESRF/ID02 beamline. The intensity shift between the experiments is due to variable sample concentrations after dialysis and addition of stabilizer.

To assess quantitatively this structural information, we have fitted the SAXS patterns with a model describing nanoparticles of adjustable surface roughness (Figure 4, red lines, and Figure 5). To account for the TEM observations, the surfaces of the particles are constructed by accumulation of N_{grain} nanometer-scaled surface primary grains (Figure 5). The total contribution is described with the following generic model (Supporting Information):

$$I(q) = \bar{n}_{\text{particle}} \Delta\rho^2 S_{\text{particle-particle}} \Big(< v^2_{\text{particle}} f^2_{\text{particle}} >_{\text{particle}} (q) + N_{\text{grain}} S_{\text{grain-grain}}(q) < v^2_{\text{grain}} f^2_{\text{grain}} >_{\text{grain}} (q) \Big) \quad \text{(Eq. 1)}$$

where $\bar{n}_P$ is the number of particles per volume unit of solution, and $\Delta\rho = \rho_{\text{crystal}} - \rho_{\text{water}}$ the contrast in scattering length density of the bulk crystal, where the scattering length density of either phase is related to the electron density μ_i via $\rho_{\text{i}} = l_T \mu_{\text{i}}$ with l_T the scattering length of a single electron. The expression is built by combining a description for the contribution of the whole particle, and a description for the aggregation of the grains within the nanoparticles. [30] The whole particle is described by phenomenological form factor $< v^2_{\text{particle}} f^2_{\text{particle}} >_{\text{particle}}$ weighted by volume and averaged over the size distribution of the particles, that describes the smooth geometrical envelope of the particles (see Fig. 5) characterized by the inflexion at $q \approx 10^{-2}$ Å^{-1}:[31]

$$< v^2_{\text{particle}} f^2_{\text{particle}} >_{\text{particle}} (q) = g \exp\left(-\frac{q^2 r^2_{g,\,\text{particle}}}{3} \right) + b q^{*-p} \quad \text{(Eq. 2)}$$

with $r_{g,\text{particle}}$ the radius of gyration of the particle and $q^* = q/\text{erf}\left(\frac{q r_{g,\,\text{particle}}}{\sqrt{6}}\right)^3$ a correction to damp the q^{-p} power law at low-q values and avoid the Guinier contribution to become negligible. Note that $\sqrt{g}$ is the volume of the geometrical envelope of the particle. The contribution of the

primary grains is described by a Gaussian distribution of spherical particles, characterized by the inflexion at $q \approx 10^{-1}$ Å^{-1} [32]:

$$< v_{\text{grain}}^2 f_{\text{grain}}^2 >_{\text{grain}} (q) = \frac{8\pi^2}{q^6}\left[1 + \lambda^2 + \mu^2 - (\text{c} + \text{s})\exp(-2\mu^2)\right] \text{(Eq. 3)}$$

with $\lambda = qr_{\text{grain}}$, $\mu = q\sigma_{\text{grain}}$, $c = [(1 + 2\mu^2)^2 - \lambda^2 - \mu^2]\cos 2\lambda$, and $s = 2\lambda(1 + 2\mu^2)\sin 2\lambda$.

The form factor of the primary grains is modulated by the structure factor describing the aggregation into the surface of the nanoparticles ($S_{\text{grain-grain}}$, see Supporting Information), producing the cross-over between the inflexions at $q \approx 10^{-2}$ Å^{-1} and $q \approx 10^{-1}$ Å^{-1}:

$$S_{\text{grain-grain}}(q) = \max\left(0,\ 1 - 9\phi_b \frac{\Gamma(5-D_s)}{(2\lambda)^{6-D_s}} \frac{1}{\left(1+(qr_{\text{particle}})^{-2}\right)^{\frac{5-D_s}{2}}} \frac{\sin[(5-D_s)\arctan qr_{\text{particle}}]}{3-D_s}\right) \text{(Eq. 4)}$$

This structure factor has been constructed using the concept of surface fractals made by accretion of grains, defined as follows (Figure 5): [33, 34] given a probe molecule of size *t*, we define the boundary volume as the total volume that the probe molecule is able to explore, while keeping in contact with the surface. For a flat surface, the volume of the boundary layer is simply $V_b = St$, with *S* the surface area of the surface. In other words, for a flat surface the V_b/t ratio give the surface area, in this case independent on the choice of the probe length *t*. The flat surfaces produce a characteristic scattering that follows a Porod's law $I \propto q^{-4}$ (Fig. 4, dotted line).

The deviations from the Porod's law observed here are assigned to the presence of rough fractal surfaces. In this case, smaller molecules will access the smaller deteails of the rough surface, while large molecules will only access a coarse-grained surface, and therefore a smaller effective area. More precisely, the boundary volume has a slower increase with *t* and varies instead as $V_b \propto t^{3-D_s}$, where $2 \leq D_s < 3$ is the fractal dimension of the surface. It results that the surface area accessible to a probe (molecule) of size *t* is:

$$A = V_b/t \propto t^{2-D_s} \qquad \text{(Eq. 5)}$$

Here, we further construct the surface fractal by accumulation of surface primary grains of diameter d_{grain} ($S_{\text{grain-grain}}$), which limits the range of the fractal behavior of eq. 2 to typically $d_{\text{grain}} \leq t \leq d_{\text{particle}}$.

In practice, we measure the surface area A per volume of geometrical envelope V as:[34]

$$\sigma = \frac{A}{V} = \frac{Iq^4}{2\pi\Delta\rho^2\bar{n}_{\text{particle}}\sqrt{g}} \text{ (Eq. 6)}$$

and fix the lower boundary to $\sigma_{\text{min}} = \frac{3}{\sqrt{\frac{5}{3}}R_{g,\text{particle}}}$, where $\sqrt{\frac{5}{3}}R_{g,\text{particle}}$ translates the radius of gyration as determined by model fitting, into the physical radius of the particle assumed spherical.

At larger probe sizes (typically > 10 nm), the surface area scales inversely with the size of the particle as usual (Figure 6). At smaller probe sizes (typically in the Angstrom range), the finer details of the particles are resolved, and the resulting surface area is the accumulation of the surface areas of the primary grains, modulated by their coalescence.

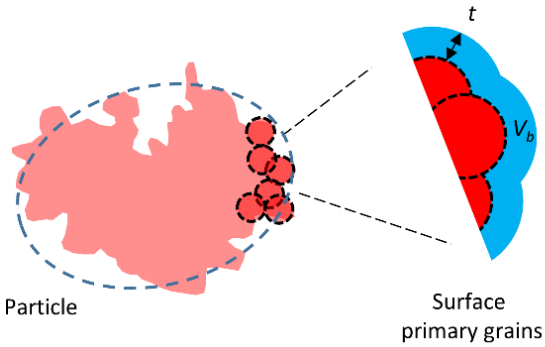

Figure 5. Construction of the model used to represent the particles for SAXS fitting. The rough surfaces are constructed by accumulation of nanometer-scaled spherical primary grains into a

surface fractal. The blue area is the boundary volume V_b delimited by a boundary thickness t, that varies as t^{3-D_s}.

Fitting the model given by eq. 1-4 to the scattering signal (see Supporting Information), we find characteristic sizes of the surface primary grains that are consistent with the TEM observations (Table 3). The surface of the YV2 nanoparticles is best described as fractal aggregates of c.a. 1 nm diameter primary grains, against 2 nm for the YV2C and YV3C samples. By contrast, for the YV3 particles, the characteristic size of the surface primary grains is found in the Angstrom range; this is consistent with the surface of the YV3 nanoparticles appearing smoother by TEM.

Sample	Mean radius of gyration / equivalent diameter (nm)	Mean primary grain diameter (nm)	D_s
YV2	16 / 41	1.9	2.65
YV3	32 / 80	0.1	2.84
YV2C	27 / 69	2.5	2.57
YV3C	23 / 58	2.4	2.74

Table 3. Summary of the physical parameters extracted after model fitting

Furthermore, we unveil how the effective specific area of the nanoparticles vary with the probe size (Eq. 5-6, Figure 6). As expected, the accessible surface area per particle decreases as the length of the probe decreases. The nanometer-sized primary grains increase the surface area by more than a factor of 10 with respect to the smooth envelope of the particles. In addition, the

YV2, YV2C and YV3C particles present surface to volume ratio c.a. 10 times as high as the YV3 particles at probe lengths below the nanometer range, and tend to become equal above.

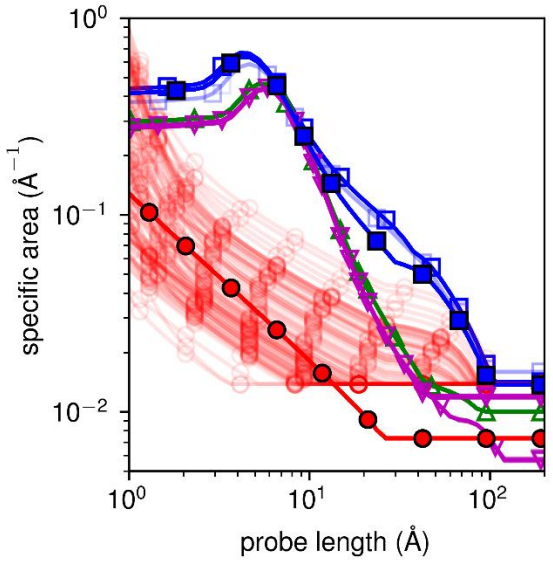

Figure 6. Surface area accessible to a probe of given size, per volume unit of nanoparticle. Blue squares: YV2; red circles: YV3; green upward triangles: YV2C; and magenta downwards triangles: YV3C. For YV2 and YV3, SAXS datasets from experiments carried out at SOLEIL/Swing (full symbols) and ESRD/ID02 (hollow symbols) have been used. For the YV3 dataset at ESRF (hollow red circles), the superimposition of graphs represents the confidence intervals. For all other datasets, the confidence interval is within the thickness of the line.

In summary, comparison of the XRD, TEM images and SAXS patterns support directly that the low-pH and carbonated syntheses yield dense and rough particles made by aggregation of primary grains (YV2, YV2C and YV3C). The YV3 particles appear smoother at the nanometer-scale with a coherence domain across the whole particle, but also present a high specific area at the Angstrom scale. The low-pH and carbonated samples (YV2, YV2C, YV3C) can be seen as resulting from the aggregation of primary grains that have partially coalesced into crystalline

domains which sizes correspond to coherence lengths shown on Table 2; on the other hand, in the particles made at high pH (YV3), the number of primary grains is below the detection limit of both TEM and the SAXS modelling, and the coherence domain propagate across the whole particle; but the large residual interfacial area stems from residuals defects remaining at the surface after the growth of the crystal domain.

The origin of these microstructures has to be found in the mechanism of the particles' formation. Previous results [18] obtained starting form an orthovanadate precursor showed that particles are formed through the crystallization of an amorphous hydroxylated phase. The difference of microstructure observed in the present work, especially considering the YV3 particles, is expected to arise from a difference in the kinetic of the crystallization process, which is found to be much slower when increasing the number of hydroxyl equivalent as compared to the metavanadate precursor. Nevertheless, another possible reason could be that a common mechanism of particles formation leads to particles formed by the aggregation of primary particles and further evolve through an intra-particulate Oswald ripening. For some reasons, the kinetics of the reconstruction would be enhanced in the case of the YV3 particles leading to their complete recrystallization into monocrystals. In this alternative scenario, the YV2 particles could be seen as intermediate states of YV3 particles during an ageing process of reconstruction. Investigations are under way to apply the methodology of SAXS/WAXS characterization developed in the present work for the characterization of the intermediate states during the particles' formation.

Summary and Conclusions.

This work aimed in revisiting the synthesis by aqueous co-precipitation of YVO4:Eu nanoparticles . The first objective was to determine the experimental conditions allowing to have a controlled and reproducible particles microstructure. The second objective was to precisely characterize the particle internal microstructure. Starting from observations of the poor reproducibility of previously reported syntheses, we focused on the precipitation using a metavanadate precursor combined with a controlled amount of base (NaOH) and sodium carbonates. This was shown to drastically affect the particles' surface while maintaining a size of approximatively 50 to 80 nm. In addition to conventional techniques (TEM, XRD), particles were fully characterized using SAXS-WAXS and a suitable methodology of data analysis to provide an accurate description of the particles' structure. Particles obtained using 3 equivalents of NaOH (YV3) were clearly different from other samples since they appeared as facetted and almost monocrystalline. Other particles, obtained with lower amount of base or with addition of carbonates, appear to be dense and polycrystalline, well described using a surface fractal description. These particles appear as resulting from the ageing of aggregates of nanometer-scaled primary grains. Further work will be devoted to the understanding of the origin of the observed microstructures by considering the mechanism of the particle formation that occurs from an amorphous to crystalline phase transition. This will be done by analyzing the evolution of the particles' formation and ageing through *in situ* monitoring of their structure. Another perspective of this work is the investigation of the influence of the particles microstructure on their properties, especially considering their emission properties and their sensitivity when being considered for application as chemical sensors.

,

AUTHOR INFORMATION

Corresponding Authors

*Thierry Gacoin – thierry.gacoin@polytechnique.edu

*David Carrière – david.carriere@cea.fr

Present Addresses

† Département NuMa, Agence Nationale de la Recherche, 50 avenue Daumesnil, 75012 Paris

Laboratoire de Génie Chimique, Université de Toulouse, CNRS, INPT, UPS, Toulouse, France

Author Contributions

§ These authors contributed equally

The manuscript was written through contributions of all authors. All authors have given approval to the final version of the manuscript.

Funding Sources

The authors acknowledge the ESRF synchrotron for beamtime. All authors acknowledge a public grant overseen by the French National Research Agency (ANR), project DIAMONS ANR-14-CE08-0003. RKR acknowledges support by ANR as part of the "Investissements d'Avenir" program (Labex NanoSaclay, reference: ANR-10-LABX-0035).

ACKNOWLEDGMENT

The authors wish to thank Blaise Fleury for fruitful discussions and preliminary results.

ASSOCIATED CONTENT

Supporting Information for publication.

- Supplementary Information : XRD analysis and derivation of the SAXS treatment (pdf)

REFERENCES

[1] Blasse, G.; Grabmeier, B. C. Luminescent Materials; Springer-Verlag: Berlin, 1994.

[2] Ropp, R. C. Luminescence and the Solid State; Elsevier: Amsterdam, 1991.

[3] Riwotzki, K.; Haase, M. Wet-Chemical Synthesis of Doped Colloidal Nanoparticles: YVO_4:Ln (Ln = Eu, Sm, Dy). J. Phys. Chem. B 1998, 102, 10129-10135.

[4] Huignard, A.; Gacoin, T.; Boilot, J.-P. Synthesis and Luminescence Properties of Colloidal YVO_4:Eu Phosphors. Chem. Mat. 2000, 12, 1090-1094.

[5] Yu, M.; Lin, J.; Wang, Z.; Fu, J.; Wang, S.; Zhang, H.J.; Han, Y.C. Fabrication, patterning, and optical properties of nanocrystalline YVO_4 : A (A = Eu^{3+}, Dy^{3+}, Sm^{3+}, Er^{3+}) phosphor films via sol-gel soft lithography. Chem. Mat. 2002, 14(5), 2224-2231.

[6] Dantelle, G.; Fleury, B.; Boilot J.-P.; Gacoin, T. How to Prepare the Brightest Luminescent Coatings? Acs Appl. Mat. & Interf. 2013, 5(21), 11315-11320.

[7] Bouzigues, C.; Gacoin, T.; Alexandrou, A. Biological Applications of Rare-Earth Based Nanoparticles. ACS Nano, 2011, 5(11), 8488–8505.

[8] Shen, J.; Sun, L.-D.; Zhu, J.-D.; Wei, L.-H.; Sun, H.-F.; Yan, C.-H. Biocompatible Bright YVO_4:Eu Nanoparticles as Versatile Optical Bioprobes. Adv. Funct. Mat. 2010, 20, 3708-3714.

[9] Duée, N. ; Ambard, C.; Pereira, F. ; Portehault, D. ; Viana, B. ; Vallé, K. ; Autissier, D. ; Sanchez, C. New Synthesis Strategies for Luminescent YVO_4:Eu and $EuVO_4$ Nanoparticles with H_2O_2 Selective Sensing Properties. Chem. Mater. 2015, 27(15), 5198-5205.

[10] Abdesselem, M.; Schoeffel, M.; Maurin, I.; Ramodiharilafy, R.; Autret, G.; Clément, O.; Tharaux, P.-L.; Boilot, J.-P.; Gacoin, T.; Bouzigues, C.; Alexandrou, A. Multifunctional Rare-Earth Vanadate Nanoparticles: Luminescent Labels, Oxidant Sensors, and MRI Contrast Agents. ACS Nano 2014, 8 (11), 11126–11137.

[11] Mialon, G.; Turkcan, S.; Alexandrou, A.; Gacoin, T.; Boilot, J.-P. New Insights into Size Effects in Luminescent Oxide Nanocrystals. J. Phys. Chem. C, 2009, 113, 18699-18706.

[12] Maurin, I.; Dantelle, G.; Boilot, J.-P. Gacoin, T. A protected annealing process for the production of high quality colloidal oxide nanoparticles with optimized physical properties. J. Mater. Chem. C, 2013, 1, 13-22.

[13] Wu, H.; Xu, H.; Su, Q.; Chen, T.; Wu, M. Size- and shape-tailored hydrothermal synthesis of YVO_4 crystals in ultra-wide pH range conditions. J. Mat. Chem. 2003, 13, 1223-1228.

[14] Wu, X.; Tao, Y.; Song, C.; Mao, C.; Dong, L.; Zhu, J. Morphological Control and Luminescent Properties of YVO_4:Eu Nanocrystals. J. Phys. Chem. B 2006, 11, 15791-15796.

[15] Ray, S.; Banerjee, A.; Pramanik, P. A novel rock-like nanoarchitecture of YVO4:Eu3+ phosphor: selective synthesis, characterization, and luminescence behavior. J. Mater. Sci. 2010, 45, 259–267.

[16] Xu, Z.; Kang, X.; Li, C.; Hou, Z.; Zhang, C.; Yang, D.; Li, G.; Lin, J. Ln3þ (Ln = Eu, Dy, Sm, and Er) Ion-Doped YVO_4 Nano/Microcrystals with Multiform Morphologies: Hydrothermal Synthesis, Growing Mechanism, and Luminescent Properties. Inorg. Chem. 2010, 49, 6706–6715.

[17] Yang, E.; Li, G.; Zheng, J.; Fu, C.; Zheng, .;Li, L. Kinetic Control over YVO4:Eu3+ Nanoparticles for Tailored Structure and Luminescence Properties. J. Phys. Chem. C 2014, 118, 3820−3827.

[18] Fleury, B.; Neouze, M.-A.; Guigner, J.-M.; Menguy, N.; Spalla, O.; Gacoin, T.; Carriere, D.; Amorphous to Crystal Conversion as a Mechanism Governing the Structure of Luminescent YVO4:Eu Nanoparticles ACS Nano 2014, 8, 2602-2608.

[19] Narayanan, T.; Sztucki, M.; Van Vaerenbergh, P.; Léonardon, J.; Gorini, J.; Claustre, L.; Sever, F.; Morse, J.; Boesecke, P. A Multipurpose Instrument for Time-Resolved Ultra-Small-Angle and Coherent X-Ray Scattering. J Appl Crystallogr 2018, *51* (6), 1511–1524.

[20] David, G. ; Pérez, J. Combined sampler robot and high-performance liquid chromatography: a fully automated system for biological small-angle X-ray scattering experiments at the Synchrotron SOLEIL SWING beamline. J. Appl. Crystallogr. 2009, 42, 892–900.

[21] Bollen, K. A. & Long, J. S. Testing Structural Equation Models. (SAGE, 1993)

[22] Baes, C.F.; Mesmer, R. S. The Hydrolysis of Cations. John Wiley & Sons: New York, London, Sydney, Toronto 1976, pp. 210, 411.

[23] Jolivet, J.-P. ; Henry, M.; Livage, J. De la solution à l'oxyde: Condensation des cations en solution aqueuse, chimie de surface des oxydes. InterEditions : Paris 1994.

[24] Chakoumakos, B. C.; Abraham, M. M.; Boatner, L. A. Crystal structure refinements of zircon-type MVO4 (M= Sc, Y, Ce, Pr, Nd, Tb, Ho, Er, Tm, Yb, Lu) J. Solid State Chem. 1994, 109, 197−202.

[25] Halder, N. C.; Wagner, C. N. J. Advances in X-Ray Analysis ; Springer, Boston, MA, 1966; pp 91-102.

[26] Halder N. C.; Wagner C. N. J. Separation of Particle Size and Lattice Strain

in Integral Breadth Measurements, Acta Crystallogr. 1966, 20, 312-313.

[27] Lutterotti, L.; Scardi, P. Simultaneous Structure and Size–Strain Refinement by the Rietveld Method. J. Appl. Crystallogr. 1990, 23, 246-252.

[28] Baglio, J. A.; Gashurov, G. A refinement of the crystal structure of yttrium vanadate. Acta Cryst. 1968, B24, 292-293.

[29] Errandonea, D.; Lacomba-Perales, R.; Ruiz-Fuertes, J.; Segura, A.; Achary, S. N.; Tyagi A. K. High-pressure structural investigation of several zircon-type orthovanadates Phys. Rev. B 2009, 79, 184104.

[30] Sen, D.; Spalla, O.; Belloni, L.; Charpentier, T.; Thill, A. Temperature Effects on the Composition and Microstructure of Spray-Dried Nanocomposite Powders. Langmuir 2006, 22, 3798–3806.

[31] Beaucage, G. Small-angle scattering from polymeric mass fractals of arbitrary mass-fractal dimension. Journal of Applied Crystallography 29, 134–146 (1996).

[32] Fleury, B.; Cortes-Huerto R.; Taché O.; Testard F.; Menguy N.; Spalla O. Gold Nanoparticle Internal Structure and Symmetry Probed by Unified Small-Angle X-ray Scattering and X-ray Diffraction Coupled with Molecular Dynamics Analysis. Nano Lett. 2015, **15**, 6088–6094.

[33] Wong, P. -Z.; Bray, A. J. Small-angle scattering by rough and fractal surfaces. J. Appl. Crystallogr. 1988, 21, 786–794.

[34] Besselink, R.; Stawski, T. M.; Van Driessche, A. E. S.; Benning, L. G. Not Just Fractal Surfaces, but Surface Fractal Aggregates: Derivation of the Expression for the Structure Factor and Its Applications J. Chem. Phys. 2016, 145 (21), 211908.

SYNOPSIS (Word Style “SN_Synopsis_TOC”). If you are submitting your paper to a journal that requires a synopsis, see the journal’s Instructions for Authors for details.